Science
AAAS

Supplementary Materials for

Orbital magnetoresistance in the antiferromagnet CoO driven by dynamic orbital angular momentum

Christin Schmitt *et al*.

Corresponding authors: Sachin Krishnia, skrishni@uni-mainz.de; Mathias Kläui, klaeui@uni-mainz.de

Science **393**, 76 (2026)
DOI: 10.1126/science.adw1808

The PDF file includes:

1 Materials and Methods

1.1 Sample growth and preparation

This section describes the growth and structural characterization of our CoO thin films. The CoO(5 nm) films were grown on MgO(001) substrates using reactive magnetron sputtering in an *ULVAC QAM 4* fully automated sputtering system. The sputtering chamber was maintained at a base pressure better than 1.2×10^{-5} Pa. Prior to deposition, the MgO substrates were pre-heated to a temperature of 770 °C for two hours. After cooling, CoO was deposited from a Co target in a mixed atmosphere of Ar (15 sccm) and O_2 (2 sccm) at a temperature of 573 °C using an RF power of 150 W. Following deposition and cooling down, non-magnetic metal layers such as Cu, Cr and Pt were deposited in-situ without breaking the vacuum at room temperature, utilizing a separate chamber and DC magnetron sputtering. The lattice constant and growth quality of CoO thin films are determined by using a Bruker D8 Discover high-resolution X-ray diffractometer.

1.2 Device fabrication and magneto-transport measurements

The as-grown samples were cleaned with acetone and isopropanol prior to patterning. The structures were patterned by photolithography using a DMO MicroWriter ML3 with negative photoresist and subsequent etching using Ar+ ion-milling technique. The Hall bar geometry consists of a 6 µm wide bar and two 2 µm wide wires perpendicular to it, separated by 6 µm and patterned along the sample's magnetic hard axes. For the CoO(5 nm)/Cu(6 nm) sample we grew CoO(5 nm)/Cu(6 nm)/Pt(2 nm) and prior to the measurements removed the Pt by argon etching for 8 s. For the electrical measurements, the sample was mounted onto a piezo-rotating element within a variable temperature insert (VTI) installed in a superconducting coil capable of generating magnetic fields up to 15 T. For field-sweep experiments, the magnetic field was swept in-plane along the two perpendicular magnetic easy axes. For angular-dependent measurements, a constant magnetic field was rotated in-plane. A charge current of 105 µA was applied to the 6 µm wide bar using a Keithley 6221 current source, alternating between positive and negative polarity. The resulting transverse and longitudinal voltage signals were detected in two transverse bars using a Keithley 2182A nanovoltmeter. The voltage value is an average of 100 measurements, with each measurement being the average of positive

and negative current polarity. The error bars are the standard deviation of these measurements. The applied current followed a square-wave signal as a function of time. A delay was introduced between the current reversal and the start of data acquisition to avoid capturing rise-time effects from the current source or capacitor-like effects in the Hall structures. By calculating the difference between the two signals arising from positive and negative current polarities, thermal contributions, such as the spin Seebeck effect, are averaged out. The resulting voltage variation was recorded as a function of the externally applied magnetic field and the angle between the charge current and the magnetic field. We define the MR amplitude as

$$\Delta R_{xy}/\bar{R} = [R_{xy}(\boldsymbol{n}_2) - R_{xy}(\boldsymbol{n}_1)]/\bar{R} \tag{S1}$$

where $\boldsymbol{n}_{1,2}$ are two orthogonal Néel vector orientations along the two magnetic easy axes $[1\bar{1}0]$ and $[110]$, respectively. $\bar{R}$ is the longitudinal resistance averaged for the two states. The measurements were performed with the electrical current $\boldsymbol{I} \parallel [100]$ crystallographic direction. The sign of the MR is defined as positive if upon reorientation of the Néel vector from $[\bar{1}10]$ to $[110]$, the transverse resistance increases, while a decrease in transverse resistance upon reorientation is defined as a negative MR.

2 Characterization of structural and crystallographic properties of CoO thin films

To determine the crystallographic orientation, lattice constant and the growth quality of our CoO thin films, we performed X-ray diffraction (XRD) measurements using a Bruker D8 Discover high-resolution diffractometer with Cu K_α radiation ($\lambda = 0.154\,06$ nm). Figure S1(a) shows the coupled $\theta - 2\theta$ scan for MgO(001)//CoO(5 nm)/Cu(6 nm). The observed peak position for CoO is consistent with the CoO(002) direction, in alignment with the orientation of the MgO(001) substrate. The position of CoO(002) is slightly shifted relative to the expected bulk value, suggesting that the CoO thin film is strained. This strain arises from a lattice mismatch of 1.1% between the bulk lattice constants of MgO substrate ($a = 0.4212$ nm) and CoO ($a = 0.4260$ nm). Figure S1(b) presents the rocking curves for the CoO(002) thin film and MgO(002) substrate peaks. Both curves exhibit similar full-width-at-half-maximum (FWHM) values, indicating the high crystalline quality of the

CoO film, with minimal dislocations, mosaicity, and defects. Moreover, the CoO peak is centered at the expected position of the film's Bragg reflection, highlighting the excellent lattice alignment between the film and substrate.

To assess the structural quality of the CoO/Cu* heterostructure, scanning transmission electron microscopy (STEM) with a high-angle annular dark-field detector (HAADF) and electron energy-loss spectroscopy (EELS) measurements were performed, as shown in Figs. S2 and S3. Cross-sectional lamellas were prepared using a Thermo Fisher Scientific (TFS) dual beam Helios system. To prevent surface damage during focused ion beam sputtering, a protective C layer was deposited using electron beam induced deposition prior to FIB milling. HAADF-STEM and EELS were conducted using a TFS Spectra TEM operated at 300 kV and equipped with a Gatan Continuum imaging filter (GIF). The HAADF-STEM image in Fig. S2(a) reveals coherent epitaxial growth of the CoO layer on the MgO substrate, confirming its high crystalline quality. The fast Fourier transform (FFT) pattern shows that the Cu layer also maintains an epitaxial relationship with the underlying CoO layer indicating a well-defined interface that facilitates the epitaxial growth on top of the CoO. The observed peak splitting indicates a relaxation of the epitaxial strain in the Cu layer. The map in Fig. S2(b) shows the variation of the horizontal lattice spacing in the stack, obtained through geometrical phase (GPA) analysis of the image in (a) and calculated with respect to the MgO substrate. At the CoO/Cu interface, lattice distortions with a periodicity of approximately 1.3 nm, indicate that the strain is accommodated through a regular array of misfit dislocations.

Figs. S3(a,b) show EELS elemental maps and corresponding atomic fraction profiles extracted along the growth direction. The O-map and profile (green) confirm the oxidation of the top Cu with an oxide layer thickness of 2.3 ± 0.3 nm.

3 Measurements of orbital magnetization in CoO thin films

In order to probe the orbital moment in our CoO thin films, we performed X-ray magnetic linear dichroism photoemission energy microscopy (XMLD-PEEM) measurements. A direct experimental quantification of orbital moments in antiferromagnetic oxides is very challenging. As CoO is an ordered antiferromagnet and a correlated Mott insulator, the $2p \rightarrow 3d$ transitions exhibit strong

multiplet splitting due to intra-atomic Coulomb and exchange interactions, therefore, the XMCD and XMLD sum rules are not applicable. Moreover, the Co ions experience a strong octahedral crystal field in the lattice, which mixes the spin and orbital characters in the ground state. In addition, hybridization between Co *3d* and O *p* states delocalizes the magnetic charge, making the sum rules also not applicable.

Therefore, we used an inverse approach to quantify the unquenched orbital moment in our CoO thin films. We measured energy-dependent X-ray absorption (XAS) in the CoO thin films and compared these experimental results with multiplet calculations of the $2p \rightarrow 3d$ transition and simulations of the expected XMLD signal for different spin and orbital moments. Such calculations can be found in the literature and have been conducted, for example, by Csiszar et al. (*57*) and Abrudan et al. (*58*). They also found a large orbital moment in their CoO films (*57, 58*).

We show our experimental data in Fig. S4. Comparing the data with the XMLD spectrum measured by Abrudan et al., we find the same key features, underlining the existence of a large unquenched orbital moment in our thin films (larger than 1 μ_B/atom).

The dichroic signal reflects how crystal field splitting and spin–orbit coupling (SOC) mix otherwise degenerate *d*-orbitals. When the orbital moment is fully quenched ($L = 0$), the XMLD spectrum is smooth and only shows basic anisotropy. However, if SOC and incomplete crystal field quenching allow for a residual orbital angular momentum, transitions into spin–orbit coupled multiplets create interference ("beating") patterns in the spectrum (*59, 60*). These modulation leads to non-monotonic variations in the intensities between 776.0 eV and 779.5 eV at the L_3 edge of Co in our measurements, serve as a sensitive fingerprint of large unquenched orbital angular momentum, since XMLD directly probes anisotropic charge and spin–orbit distributions rather than net magnetization. Therefore, these measurements, together with comparisons to previous studies on CoO thin films, underline the presence of a large enhanced unquenched orbital moment (larger than 1 μ_B/atom as seen from the comparison to literature) in our samples, which facilitates the observed giant orbital magnetoresistance.

4 OMR measurements of CoO/Cr

To understand the universality of the observed mechanism and in particular to check if the observed mechanism is specific to oxidized Cu, or can be observed with other orbital angular momentum generating materials, we have conducted additional experiments using the weak SOC material Cr. We performed experiments analogous to those on CoO/Cu* on MgO//CoO(5 nm)/Cr(13 nm)/Al_2O_3(5 nm). The samples were capped with Al_2O_3 to prevent them from surface oxidation. The thickness of CoO was chosen to match that used in the CoO/Cu* experiments and the thickness of Cr was chosen considering its orbital diffusion length of approximately 6.5 nm (*61*). We have chosen Cr as it is predicted to exhibit large orbital Hall conductivity and is known to exhibit a very small spin Hall conductivity (*22, 28*).

As a key result, we find that using Cr as an orbital angular momentum generator, a large signal is found that cannot be explained by a spin Hall effect but results from an orbital degree of freedom analogous to the results with Cu*. Using Cr allows us to determine the orientation of the Néel vector of the orbital magnet CoO by following the same experimental procedure detailed in the main manuscript. Analogous to Fig. 2(b) of the main manuscript for CoO/Cu*, in Fig. S5(a), we show R_{xy}, normalized by the longitudinal resistance i.e. OMR, as a function of in-plane magnetic field in the CoO/Cr sample at a temperature of $T = 250\,\mathrm{K}$. We observe an abrupt change in R_{xy} around 11 T magnetic field, corresponding to the spin-flop field of CoO in this sample. These experiments confirm that we can read the orientation of the Néel vector in our CoO thin films using the weak SOC material Cr, in which the spin Hall effect is negligible (*22, 28*). Above $T = 300\,\mathrm{K}$ no spin-flop is observable anymore, further validating the magnetic origin of the measured signal.

To understand whether the signal originates from the interaction between orbital current from Cr and orbital magnetization in CoO, we measured the OMR as a function of temperature and compared its magnitude with that of SMR in CoO/Pt. Figure S5(b) shows an increase of $R_{xy}/\bar{R}$ in the CoO/Cr sample as the temperature decreases. At $T = 150\,\mathrm{K}$, $R_{xy}/\bar{R}$ is 0.033%, which is ~5 times larger than the pure SMR signal measured in CoO/Pt samples. Owing to the weak spin–orbit coupling and negligible SHE in Cr (compared to Pt) (*22, 28*), this behavior can only be explained within the framework of orbital current generation in Cr and its interaction with the orbital magnetization of CoO. The OMR in CoO/Cr exhibits the same sign as the CoO/Cu* samples,

in contrast to CoO/Pt, where it is reversed.

The observation of the many-fold enhancement of the OMR in the CoO/Cr sample clearly confirms that this effect does not rely on the oxidation and resulting poor conductivity of Cu*, but is also present in other metallic materials with weak SOC, thereby highlighting its generality and opening promising new research directions.

5 Measurements on $\alpha - Fe_2O_3/Cu^*$

To confirm that the observed effects in CoO/Cu* are originating from orbital physics, we performed MR measurements on $\alpha - Fe_2O_3$(hematite)$/Cu^*$. Hematite has a nearly quenched OAM and is thus expected to show negligible response to the orbital currents (*62*). For this, we used a 100 nm thin film in c-cut orientation, interfaced with 5 nm thick Cu*. On this particular $\alpha - Fe_2O_3$ sample, we performed SMR measurements using a spin current generated in Pt, as shown in Fig. S6(a). We found that, due to the structure of this sample, SMR of the order of $\sim 3 \times 10^{-4}$ arises at low magnetic field when performing field-sweep measurements at 175 K in the easy-axis phase (see also Ref. (*63*)).

We patterned Hall bars equivalent to those used for the measurements on CoO and injected electrical currents up to 1 mA, to ensure a good signal-to-noise ratio. We applied the magnetic field parallel to the direction of the electric current. We observed no significant change in the resistance at low magnetic fields (up to 2 T). Only at high magnetic fields, a resistance change in the order of $\sim 2 \times 10^{-4}$ is observed. However, as this magnetic field strength is far above the spin-flop field of $\alpha - Fe_2O_3/Cu^*$, the origin of this signal cannot be magnetic from the hematite. Thus, we confirm that the observed giant OMR in CoO/Cu* originates from the interaction between the orbital current and the unquenched OAM of CoO.

6 Cu thickness determination

To ensure maximum comparability of the Cu* thickness dependence on OMR, all Cu* thickness dependence measurements were performed on the same Hall bar device. This approach minimizes the impact of any potential variation arising from the CoO/Cu* interface due to growth conditions

on the measured OMR. The Cu* thickness was progressively reduced by using repeated Ar-ion etching of the Hall bar device used for the electrical measurements to study the OMR. After each etching step, the precise Cu* thickness was determined by measuring the sheet resistance of the Cu* layer and comparing it with the sheet resistances of as-grown films of known Cu* thicknesses. For the as-grown samples with varying Cu* thicknesses, we used the Van der Pauw method (*64*) to determine the sheet resistance (R_S). For the etched Hall bar structure, we measured the longitudinal resistance at room temperature and accounted for the device geometry ($w = 6\,\mu$m, $l = 8\,\mu$m) by dividing it by a factor of 1.33. Fig. S7 (a) shows the sheet resistance as a function of etch time. In Fig. S7 (b), we show how the sheet resistances of the etched films were matched to those of the as-grown samples. It is worth noting that a Cu* layer with a thickness of 2 nm was already fully oxidized, rendering the sheet resistance measurement impossible.

7 Angular dependent measurements on CoO/Pt and CoO/Cu*

We performed angular-dependent magnetoresistance measurements on CoO/Pt and CoO/Cu* at various external magnetic fields, ranging from below to above the spin-flop fields of CoO. A static magnetic field of up to 11 T was applied at a temperature of 200 K, and the sample was rotated in the *x*-*y* plane to vary the in-plane angle between the applied electric current and the magnetic field. The angle was varied over a range of 300° in steps of 1°. The MR of CoO/Pt and CoO/Cu* is shown in Fig. S8(a) and (b), respectively.

Our measurements reveal that, for externally applied magnetic fields below the spin-flop field (7 T), the angular scans in the *x*-*y* plane exhibit a sinusoidal variation in transverse resistance. However, when the in-plane magnetic field exceeds the spin-flop field, additional hysteresis loops emerge, centered around the hard-axis directions ([100], [010], and [$\bar{1}$00]) of the sample. These hysteresis loops can be attributed to field-induced anisotropy arising from the unquenched OAM in CoO (*38*). The different behaviour of the two signals raises questions about their origin and their respective contributions to the overall MR. To address this, we analyzed the magnetic field dependence of the transverse resistance by separating the sinusoidal and hysteretic components. We first calculated the required shift to align one branch of the hysteresis curve with the other. The magnitude of this shift corresponds to the amplitude of the hysteretic signal. Subsequently,

we fitted a $\sin^2(x)$ function to the signal to represent the data without the hysteretic contribution, thereby determining the amplitude of the sinusoidal component. The two steps are illustrated in Fig. S9. As shown in Fig. 3 of the manuscript, we find that the hysteretic signal emerges only above the spin-flop field and saturates at 9 T. In contrast, the sinusoidal contribution increases with the applied magnetic field as shown in Fig. S10. The magnetic field range for which a hysteretic signal is observed without reaching the saturated amplitude yet, corresponds well to the range of magnetic field strengths in Fig. 2(b) of the manuscript for which the spin-flop transition is observed, thus indicating that the hysteresis in the MR signal corresponds to the switching of the Néel vector. The magnitude of the hysteretic component quantifies the MR amplitude. At 200 K, the extracted MR values for the CoO/Cu* and CoO/Pt samples are 0.25% and 0.002%, respectively. These values are consistent with those obtained using the zero-field approach (see Fig. 2(c)). Consequently, the observed hysteresis in the transverse MR not only confirms the presence of significant unquenched OAM in our samples but also provides a reliable measure of the MR amplitude through the height of the hysteretic component. On the other hand, the sinusoidal signal likely arises as an artifact due to MR contributions from the Cu layer and is not of magnetic origin from the CoO.

8 Electronic structure of CoO

We performed our density functional theory (DFT) calculations of CoO using the full-potential linearized augmented plane wave method (FLAPW), as implemented in the Jülich DFT code FLEUR (*65*), with the Perdew-Burke-Ernzerhof (*66*) parametrization of the exchange-correlation potential. For the self-consistent calculations, a 16×16×16 k-point mesh was used to sample the whole Brillouin zone. To account for the effect of electron-electron correlation among $3d$-electrons of Co, the GGA+U method in Liechtenstein approach was applied within a self-consistent DFT cycle. The on-site Coulomb and Hund exchange parameters were set to U = 6.0 eV and J = 0.92 eV. We set the muffin-tin radii to 2.48 a.u. for Co and 1.4 a.u. for oxygen atoms. The cut-off for the plane-wave basis functions was chosen as $K_{\max}$ = 4.3 and $G_{\max}$ = 12.9 a.u.$^{-1}$ for the charge density and potential. The upper limit of angular momentum inside of the muffin-tin spheres was set to $l_{\max}$ = 10 and 6 for Co and O respectively.

In accordance to the experimental setup, here, we consider two directions of the Néel vector in

the unit cell: along [110] and [1$\bar{1}$0]. The corresponding spin- and orbitally-resolved band-structures are shown in Fig. S11. We predict the values of 2.63 (2.63) and 1.16 (1.11) μ_B for atomic spin and orbital moments for the [110] ([1$\bar{1}$0]) case, respectively.

9 Orbital response properties of CoO

Here, by referring to first-principles calculations, we calculate the response of the electronic subsystem to an effect of an orbital current injected through the CoO/Cu* interface into CoO. We compare the results of our calculations when the effect is driven by the injection of the spin current generated in Pt through the CoO/Pt interface. Using linear response theory, formulated in terms of bulk states of CoO, we are going to assess the change in the expectation value of an operator of interest, which we denote as $\mathcal{J}$, to an exerted by electrical current orbital or spin exchange field, which we model by a perturbation of the kind $B_i^L L_i$ or $B_i^S S_i$, where B_i^L and B_i^S quantify the strength of effective orbital and spin fields. The response of the expectation value of $\mathcal{J}$ can be written as $\delta\langle\mathcal{J}_i\rangle = \chi^L_{\mathcal{J},ij} B_j^L$ and $\delta\langle\mathcal{J}_i\rangle = \chi^S_{\mathcal{J},ij} B_j^S$, where $\chi^{L(S)}_{\mathcal{J},ij}$ is the corresponding orbital (spin) $\mathcal{J}$-response tensor:

$$\chi^{L(S)}_{\mathcal{J},ij} = -\hbar \sum_{n<E_F} \sum_{m>E_F} \mathrm{Im} \frac{\langle n|\mathcal{J}_i|m\rangle\langle m|T_j^{L(S)}|n\rangle}{(\varepsilon_n - \varepsilon_m)^2}, \tag{S2}$$

where $T_j^{L(S)}$ is the total spin or orbital torque, defined as $T_j^L = \frac{1}{i\hbar}[L_j, H]$ and $T_j^S = \frac{1}{i\hbar}[S_j, H]$, with H being the system's electronic Hamiltonian. In the latter expression the $|n\rangle$ and $|m\rangle$ are the occupied and unoccupied eigenstates of the ground state Hamiltonian with eigen energies ε_n and ε_m, and the integration over k-space is implied. In the following we focus in particular on the response of $\mathcal{J}$, where $\mathcal{J}$ is given by the Co-resolved spin and orbital angular moments, S_i and L_i, and orbital quadrupoles (OQPs), $\{L_i, L_j\}$.

The response of S_i and L_i is shown in Fig. S12 for two different directions of the Néel vector. In this figure we observe three notable features: (i) In the case of spin current (i.e. perturbation by a spin exchange field), the response of the orbital moments vanishes within the gap, and only spin moments are generated. (ii) When the system is perturbed by the orbital current (i.e. when the system is perturbed by an orbital exchange field), the response of both spin and orbital moments is non-vanishing within the gap, with the magnitude of the effect larger by an order of magnitude

than in the case of spin current. (iii) We observe a strong anisotropy of the response to the orbital current, which is absent in the case of spin current. Indeed, when the spin exchange field points along [100], the Co-resolved induced spin moments are staggered and are perpendicular to local Co spin moments, irrespective of the direction of the Néel vector, pertaining their magnitude as the Néel vector is rotated. Turning to the case of the orbital current, we observe that while for the Néel vector along [110] the induced spin moments are aligned with the local Co moments, turning the Néel vector into the $[1\bar{1}0]$ direction keeps the magnitude of the induced spin moments, but makes them antiparallel to the Co moments, which signifies a very strong anisotropic spin response. The response of the orbital moments to the orbital current is anisotropic as well: and the Néel vector is rotated, the induced orbital moments change their direction in a non-trivial way altering the magnitude as well. This is to be expected, given that the response to the orbital perturbation directly feeds off the intrinsic anisotropy of the magnetic structure in CoO as reflected e.g. in the sensitivity of the orbital moments and crystal field splittings on the direction of $\hat{\boldsymbol{n}}$, that we observe in our calculations.

The response of $\{L_x, L_y\}, \{L_x, L_z\}, \{L_y, L_z\}, L_x^2, L_y^2, L_z^2$ quadrupoles is shown in Fig. S13 for two different directions of the Néel vector. We observe the following: (i) OQPs L_x^2 and L_y^2 exhibit a qualitatively different behavior in the gap. First of all, both quadrupoles are several times larger in case of an orbital current than in case of a spin current, with L_x^2 being about 5 times larger than L_y^2. At the same time, L_x^2 is staggered and insensitive to the Néel vector direction, while staggered L_y^2 changes drastically when changing $\hat{\boldsymbol{n}}$. (ii) The response of L_z^2 to spin current is practically vanishing within the gap, while it is significant for the case of the orbital current. In the latter case, for this OQP the response is identical for both types of Co atoms and the anisotropy with respect to the direction of the Néel vector is very large. (iii) The response of $\{L_x, L_z\}$ and $\{L_y, L_z\}$ quadrupoles is very weak to both spin and orbital currents. For $\{L_x, L_y\}$ OQP, in case of orbital currents, where the response is several times larger as compared to spin currents, the exhibited behavior is qualitatively very similar to that of L_x^2, with the only difference that the staggered $\{L_x, L_y\}$ response changes sign on each Co as Néel vector is rotated from [110] into $[1\bar{1}0]$.

10 Effective model of quadrupole dynamics

The orbital state of CoO and coupling between the spins and orbital moments are described with the Hamiltonian

$$\hat{\mathcal{H}} = \sum_{j=1,2} \left[-K^L \left(\hat{\mathbf{L}}_j \mathbf{e}_j \right)^2 - K_{\text{an}}^{\text{ea}} \left(\hat{L}_{jX}^2 - \hat{L}_{jY}^2 \right) \left(S_{jX}^2 - S_{jY}^2 \right) + K_{\text{an}}^{\text{ha}} \left\{ \hat{L}_{jX}, \hat{L}_{jY} \right\} S_{jX} S_{jY} + \lambda \mathbf{S}_j \hat{\mathbf{L}}_j \right]. \tag{S3}$$

Here the $\mathbf{S}_j$ ($j = 1, 2$) are the magnetic spins at two magnetic sublattices, treated as the classical vectors. Operators $\hat{\mathbf{L}}_j$ describe the effective orbital angular momenta ($L = 1$) at the Co sites. The first term in Eq. (S3) describes the anisotropy of the angular momenta. The local quantization axes $\mathbf{e}_1 \downarrow\downarrow \mathbf{e}_2 \uparrow\uparrow \hat{x}$ are fixed along the equilibrium orientation of the Néel vector and opposite to the sublattice magnetizations. The next two terms describe contribution into magnetic anisotropy with values parametrized by the constants $K_{\text{an}}^{\text{ea}}, K_{\text{an}}^{\text{ha}} > 0$. The last term in Eq.(S3) describes the spin-orbit coupling with $\lambda > 0$ being the coupling constant. The orthogonal axes X and Y are parallel to the in-plane easy magnetic axes [110] and [1$\bar{1}$0] and are rotated by 45° with respect to the x, y axes used in Supplementary Information S9. We keep only the terms that include operators of the orbital moments and omit Zeeman energy which describes interaction with the external magnetic field. It is worth noting that the terms with $K_{\text{an}}^{\text{ea}}$ and $K_{\text{an}}^{\text{ha}}$ come from the crystal field and could be comparable or stronger than the spin-orbit coupling λ. However, the spin-orbit interaction cannot be neglected, since it fixes the orientation of the spin and orbital moment at the magnetic atoms (see Fig. 1(a) of the main text).

The ground states of the Hamiltonian Eq. (S3) in the basis $\{|1_j\rangle, |0_j\rangle, |-1_j\rangle\}$ of eigenfunctions of the operator $\hat{L}_X$ are

$$|\psi_{+j}\rangle = \cos\chi_j |1_j\rangle + \sin\chi_j |-1_j\rangle,\ |\psi_{-j}\rangle = -\sin\chi_j |1_j\rangle + \cos\chi_j |-1_j\rangle,\ |\psi_{0j}\rangle = |0_j\rangle, \tag{S4}$$

with the eigenenergies

$$\varepsilon_{\pm} = -K_{\text{an}}^{\text{ea}} \mp \sqrt{\lambda^2 + \left(K_{\text{an}}^{\text{ea}}\right)^2},\ \varepsilon_0 = 2K_{\text{an}}^{\text{ea}}. \tag{S5}$$

Here

$$\tan\chi_1 = \frac{K_{\text{an}}^{\text{ea}}/\lambda}{1 + \sqrt{1 + \left(K_{\text{an}}^{\text{ea}}/\lambda\right)^2}},\ \chi_2 = \frac{\pi}{2} - \chi_1. \tag{S6}$$

Since $\varepsilon_+ < \varepsilon_- < \varepsilon_0$, the ground state is $|\psi_+\rangle$. The following relations are satisfied: $\langle\psi_{+j}|\hat{L_Y}|\psi_{+j}\rangle = \langle\psi_{+j}|\hat{L_Z}|\psi_{+j}\rangle = 0$, $\langle\psi_{+1}|\hat{L}_X|\psi_{+1}\rangle = -\langle\psi_{+2}|\hat{L}_X|\psi_{+2}\rangle = \hbar\cos 2\chi_1 \neq 0$. Remarkably, the orbital moments contribute to the magnetic anisotropy (the term with $K_{\rm an}^{\rm ea}$ in (S3)), since $\langle\psi_{+j}|\hat{L}_{jX}^2 - \hat{L}_{jY}^2|\psi_{+j}\rangle = \hbar^2/2$ and $\langle\psi_{+j}|\left\{\hat{L}_{jX}, \hat{L}_{jY}\right\}|\psi_{+j}\rangle = 0$. This means that the coupling with the orbital moments removes the degeneracy of the x and y easy spin axes in the ground state.

To describe qualitatively the effect of the pumping of the orbital moment, we first assume that the orbital current induces the transition to the superposition state of $|\psi_{+j}\rangle$ and $|0_j\rangle$: $|\psi_{{\rm fin},j}\rangle = \cos\frac{\theta_j}{2}|\psi_{+j}\rangle + \sin\frac{\theta_j}{2}e^{i\varphi_j}|0_j\rangle$. The average orbital moments in the final state have nonzero components in y and z directions:

$$\begin{aligned}
\langle\psi_{{\rm fin},j}|\hat{L}_X|\psi_{{\rm fin},j}\rangle &= \hbar\cos^2\frac{\theta}{2}\cos 2\chi_j, \\
\langle\psi_{{\rm fin},j}|\hat{L}_Y|\psi_{{\rm fin},j}\rangle &= \hbar\sin\theta\sin\left(\chi_j + \frac{\pi}{4}\right)\cos\varphi_j, \\
\langle\psi_{{\rm fin},j}|\hat{L}_Z|\psi_{{\rm fin},j}\rangle &= \hbar\sin\theta\cos\left(\chi_j + \frac{\pi}{4}\right)\sin\varphi_j.
\end{aligned} \tag{S7}$$

Moreover, in this case the quadrupole $\langle\psi_{{\rm fin},j}|\{\hat{L}_{jX}, \hat{L}_{jY}\}|\psi_{{\rm fin},j}\rangle = \hbar^2\sin\theta\cos\left(\chi_j + \frac{\pi}{4}\right)\cos\varphi_j$. On the other hand, the transition to the superposition of $|\psi_{+j}\rangle$ and $|\psi_{-j}\rangle$ states only induces a change in the $\langle\hat{L}_X\rangle$ component, leaving $\langle\hat{L}_Y\rangle = \langle\hat{L}_Z\rangle = 0$, and $\langle\{\hat{L}_{jX}, \hat{L}_{jY}\}\rangle = 0$.

Next, we note that the quadrupole $\langle\{\hat{L}_{jX}, \hat{L}_{jY}\}\rangle$ contributes to the effective magnetic anisotropy of CoO, the contribution being

$$w_{\rm an} = \ldots + K_{\rm an}^{\rm ha}\left[\langle\{\hat{L}_{1X}, \hat{L}_{1Y}\}\rangle + \langle\{\hat{L}_{2X}, \hat{L}_{2Y}\}\rangle\right] n_X n_Y + \ldots, \tag{S8}$$

where we keep only the leading terms proportional to the Néel vector $\boldsymbol{n}$.

The value of the quadrupole can be estimated from Eq. (S7), assuming that $\langle\psi_{+j}|\hat{L}_Y|\psi_{+j}\rangle \propto J_Y$ is related to the orbital current J_Y of the L_Y component:

$$\langle\{\hat{L}_{1X}, \hat{L}_{1Y}\}\rangle + \langle\{\hat{L}_{2X}, \hat{L}_{2Y}\}\rangle \propto \frac{J_Y}{\cos 2\chi_1}. \tag{S9}$$

Substituting Eqs. (S8) and (S9) into the equations of magnetic dynamics for the Néel vector

$$\boldsymbol{n}\times\ddot{\boldsymbol{n}} = -\gamma^2 H_{\rm ex}\boldsymbol{n}\times\frac{\partial w_{\rm an}}{\partial\boldsymbol{n}} \tag{S10}$$

we get a current-induced torque acting on the Néel vector. Here γ is the gyromagnetic ratio, $H_{\rm ex}$ is the intersublattice exchange field that keeps the sublattice spins antiparallel. In an accepted geometry

where equilibrium $\boldsymbol{n}_{\rm eq} \uparrow\uparrow \hat{X}$, this torque produces a perpendicular in-plane component $n_Y \propto \gamma^2 H_{\rm ex} J_Y / \cos 2\chi_1$. The energy associated with the magnetic dynamics $\Delta E \propto n_Y^2 \propto K_{\rm an}^{\rm ha} J_Y^2 / \cos^2 2\chi_1$. Since only the current of the y component induces magnetic dynamics, $J_Y \propto j \sin\varphi$, where j is the charge current density and φ is the angle between the pumped orbital moment and the equilibrium orientation of the Néel vector. The magnetoresistance is then associated with the absorption of magnetic energy in CoO: $\Delta R \propto \Delta E / j^2 \propto K_{\rm an}^{\rm ha} \sin^2\varphi$.

11 Ab initio spin and orbital exchange Hamiltonian of CoO

In order to evaluate the spin and orbital intersite exchange interactions (IEI) in CoO we employed an ab initio methodology based on DFT+dynamical mean-field theory (*67–69*) and the quasi-atomic Hubbard-I (HI) approximation (*70*), referring to this approach as DFT+HI below. First, the electronic structure of CoO in the paramagnetic phase was calculated using DFT+HI. Subsequently, intersite exchange interactions (IEI) were extracted from this electronic structure using the force theorem in Hubbard-I (FT-HI) approach (*71*). We solved the resulting effective Hamiltonian in mean-field and calculated its excitation spectra within a random-phase approximation.

11.1 DFT+Hubbard-I calculations

Our DFT+HI calculations were carried out using the charge self-consistent DFT+DMFT implementation of Refs. (*72–74*) that is based on the Wien2k linearized augmented plane-wave (LAPW) full-potential code (*75*) and "TRIQS" library (*76*). We employed the experimental cubic structure of paramagnetic CoO. The local-density approximation was employed as the DFT exchange correlation functional. The Brillouin zone (BZ) integration was performed using 2000 **k** points in the full Brillouin zone. The LAPW basis cutoff $R_{\rm MIN} K_{\rm MAX}$ was set to 7. The spin-orbit coupling (SOC) was neglected in these DFT-HI calculations and in the subsequent FT-HI calculations of IEI.

The Co $3d$ correlated orbitals were represented by projective Wannier functions (*72, 77*) constructed from the manifold of Co $3d$ bands; this manifold is not entangled with other bands. We specified the rotationally-invariant on-site Coulomb interaction for Co $3d$ shell by $U = F^0 = 7$ eV and $J_H = 0.9$ eV, in accordance with cRPA estimates (*78*), which, together with the standard assumptions on the ratio of Slater parameters $F^4/F^2 = 0.625$ (*79*), fully specify the interaction

vertex.

11.2 Calculations of intersite exchange interactions

DFT+HI calculations converge to a Mott insulating paramagnetic state with the Co^{2+} ion in the d^7 high-spin ground state, in agreement with Hund's rules, as expected. It is specified by spin $s = 3/2$ and an unquenched angular momentum that can be represented by a (pseudo-)orbital angular momentum $l = 1$ (*80*). The resulting ground state (GS) multiplet with the degeneracy $(2l + 1)(2s + 1) = 12$ is energetically well separated from excited d^7 levels, with the lowest excited multiplet located at about 0.84 eV. The admixture of excited multiplets to the GS due to IEI or one-electron single-site terms can thus be neglected. Correspondingly, the effective low-energy Hamiltonian H_{eff} takes the following general form:

$$H_{\text{eff}} = H_{\text{SI}} + H_{\text{IEI}} = \sum_i H_{\text{SI}}(i) + \sum_{\langle ij \rangle} \sum_{ab} V_{\alpha\beta}(\mathbf{R}_{ij}) \Omega_i^\alpha \Omega_j^\beta, \tag{S11}$$

where i and $\langle ij \rangle$ run over the Co sites and Co-Co bonds $\mathbf{R}_{ij}$, respectively. $H_{\text{SI}}(i)$ is the single-ion term acting within the GS multiplet, which can include spin-orbit and crystal-field contributions, while the IEI term comprises all possible pair-wise interactions between spin-orbital operators Ω^α acting on the GS multiplets on corresponding Co sites. The operators Ω^α that are active in the GS manifold when SO is neglected are the spins $S(Q)$, orbital moments $L(Q)$, their products $S(Q)L(Q')$, where $Q, Q' = x, y, z$, as well as the orbital quadrupoles $L^2(P)$ and their products with spins $L^2(P)S(Q)$, where P is the standard quadrupole projection xy, yz, z^2, xz, or $x^2 - y^2$. The quadrupoles are defined in the standard way, e. g. $L^2(xy) = \left(L_x L_y + L_y L_x\right)/N$. We use the normalized operators Ω^α, i. e. the normalization N is chosen such that $Tr\left[\Omega^\alpha \cdot \Omega^\beta\right] = \delta_{\alpha\beta}$.

The IEI couplings $V_{\alpha\beta}(\mathbf{R}_{ij})$ in (S11) were calculated from the converged DFT+HI paramagnetic electronic structure within the FT-HI approach (*71*) using its implementation in the "MagInt" code (*81*). This approach derives the low-energy exchange Hamiltonian by evaluating the response of the DFT+DMFT functional (*82, 83*) to simultaneous small fluctuations within the GS multiplet density matrix (DM) ρ on two neighboring sites. The FT-HI has been extensively used to derive effective magnetic Hamiltonians for insulating magnets, in particular, for systems with strong SOC, see Ref. (*84*) for a review.

We calculated IEI couplings $V_{\alpha\beta}(\mathbf{R}_{ij})$ for all nearest-neighbor (NN) and next-nearest-neighbor (NNN) Co-Co vectors. The isotropic antiferromagnetic NNN spin-spin IEI is by far the largest (about 90 meV). However, among the NN IEIs, the largest magnitudes are found within the orbital quadrupole-quadrupole (OQQ) subblock, i. e. between $L^2(Q)$ operators. In particular, the diagonal antiferroic coupling between $L^2(z^2)$ quadrupoles is the largest (11.9 meV). Several OQQ couplings are of a comparable magnitude. A detailed description of our results on the IEI interactions in CoO will be presented elsewhere.

11.3 Magnetic excitations in bulk CoO from effective Hamiltonian

In order to validate the calculated IEI interactions, we first employed them to derive the magnetic order and ordering temperature in bulk CoO. To derive the single-ion term H_{SI}, which contains the SOC and crystal-field (CF) contributions, for bulk CoO, we ran DFT+HI calculations for its experimental monoclinic low-temperature lattice structure (*85*). In these DFT+HI calculations CoO was also considered to be paramagnetic. We used the same parameters as in our calculations of IEI, apart from the SOC being turned on. We also employed the approach of Ref. (*86*) to suppress the impact of DFT self-interaction error on the CF splitting by averaging the Boltzmann weights within the Hund's rule GS multiplet. The SO term is found to provide the dominating contribution to the on-site splitting. The effective SOC $\lambda = -4D/9 = -17.4$ meV extracted from the splitting $D = 39.2$ meV between the GS $j = 1/2$ doublet and the first excited $j = 3/2$ quadruplet in the SO-level scheme, agrees well with the value of $\lambda = -16$ meV inferred from measurements of Co^{2+} ions in an MgO host (*87*).

Having determined the full effective Hamiltonian for the bulk CoO we solve it within single-site mean-field approximation using the "McPhase" (*88*) package together with an in-house module for the single-site mean-field problem. We obtain a collinear antiferromagnetic order consistent with experimental data, (*85*), i. e. the predicted magnetic structure with the propagation vector $\mathbf{k} = [1/2, 1/2, 1/2]$ and two Co sites per unit cell consisting of ferromagnetic (111) sheets that are stacked antiferromagnetically. The total Co magnetic moment of 4.04 μ_{B} is composed of the spin and orbital contributions of 2.78 μ_{B} and 1.26 μ_{B}, respectively; the total moment is tilted by the angle $\phi = 18.3^\circ$ with respect to the pseudo-cubic c axis. This structure agrees rather well with the

experimental one, which has the same collinear type with the total moment of 3.98 μ_B (*85*) and tilting $\phi = 11.4^\circ$ (*44*).

Subsequently we calculated the excitation spectra above this mean-field ground state within the generalized random-phase approximation (RPA), see, e. g., Refs. (*89, 90*). Within this approximation, the general susceptibility matrix reads

$$\bar{\chi}(\mathbf{q}, E) = \left[I + \bar{\chi}_0(E)\bar{V}_\mathbf{q}\right]^{-1} \bar{\chi}_0(E), \tag{S12}$$

where $\bar{\chi}_0(E)$ is the on-site bare susceptibility, $\bar{V}_\mathbf{q}$ is the Fourier transform of the IEI matrices $\hat{V}(\mathbf{R}_{ij})$, the bar $\bar{..}$ designates a matrix in the combined $\mu = [\alpha, a]$ index labeling the multipoles α and the sites a within the magnetic unit cell, respectively. The on-site susceptibility $\bar{\chi}_0(E)$ is calculated from mean-field potential and H_{SI} as described, e.g., in Ref. (*90*).

In Suppl. Fig. S14(a) we show the absorptive part of the calculated susceptibility traced over the operator and site indices, $Tr\Im\bar{\chi}(\mathbf{q}, E)$, along high-symmetry directions of the parent fcc Brillouin zone of CoO. Within the displayed range below 80 meV one finds two well separated bands of excitations each consisting of two branches, with the lower dispersive band spanning the range from 25 to 55 meV, the upper much more narrow band is between 70 and 78 meV. The excitation gap of about 25 meV calculated from our ab initio effective Hamiltonian compares reasonably with the gap of 20 meV observed in experimental inelastic neutron scattering (*91, 92*). In order to identify the character of each band we also calculated the partial traces $Tr_{\mathrm{sp}}\Im\bar{\chi}(\mathbf{q}, E)$ and $Tr_{\mathrm{qorb}}\Im\bar{\chi}(\mathbf{q}, E)$ over the spin and orbital-quadrupole subblocks of $\bar{\chi}$ that are displayed in Suppl. Figs. S14(b) and S14(c), respectively. One sees that the lower band is mainly of the orbital character, while the upper one is dominated by spin excitations. The lower branch happens to be at the energy corresponding to the lowest spin-orbit excitation in our single-site level scheme, about 40 meV. We thus assign it to the spin-orbit exciton, discussed before for CoO (*92, 93*) as well as strong spin-orbit-coupled systems like the layered iridate Sr_2IrO_4 (*94*).

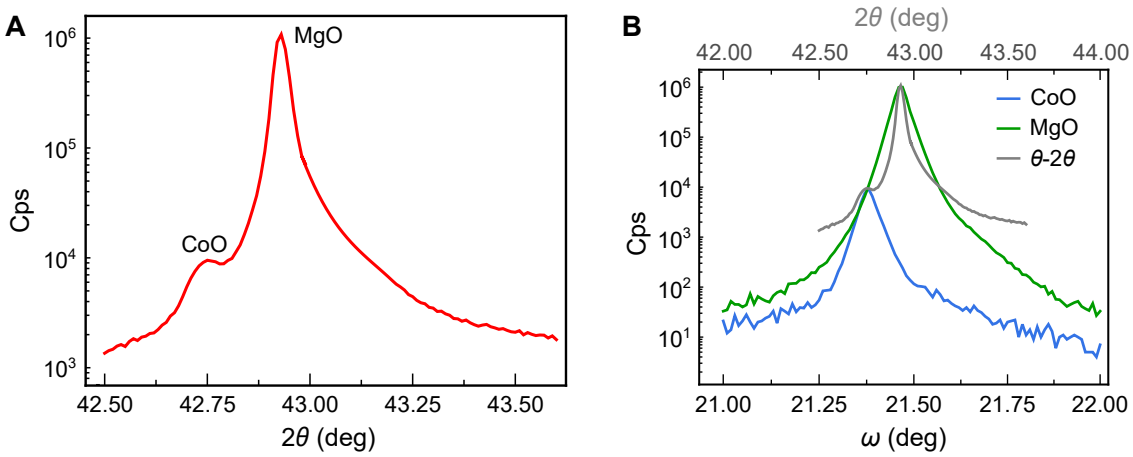

Figure S1: **Structural properties of CoO thin films grown on an MgO(001) substrate. (A)** $\theta - 2\theta$ XRD scan showing the (001) alignment of the CoO(5 nm)/Cu(6 nm) film on an MgO(001) substrate. **(B)** XRD rocking-curves of CoO(002) and MgO(002) planes on top of the $\theta - 2\theta$ scan (grey) from panel (A).

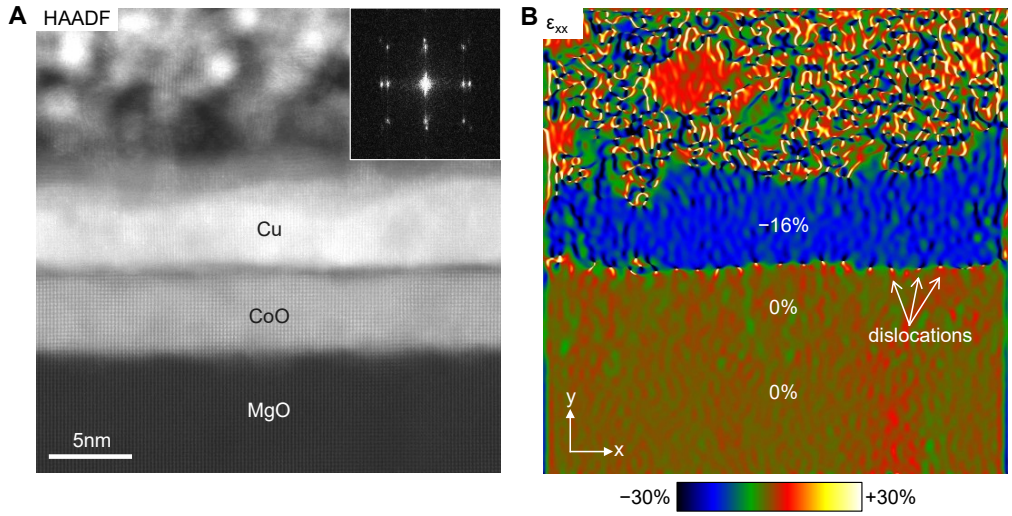

Figure S2: **(A)** HAADF STEM image with corresponding FFT in inset showing epitaxial alignment. **(B)** Horizontal deformation map calculated via geometric phase analysis. The deformation is calculated with respect to the lattice spacing of the MgO substrate following $\epsilon = (d - d_{\mathrm{MgO}})/d_{\mathrm{MgO}}$, for which d is the local lattice spacing.

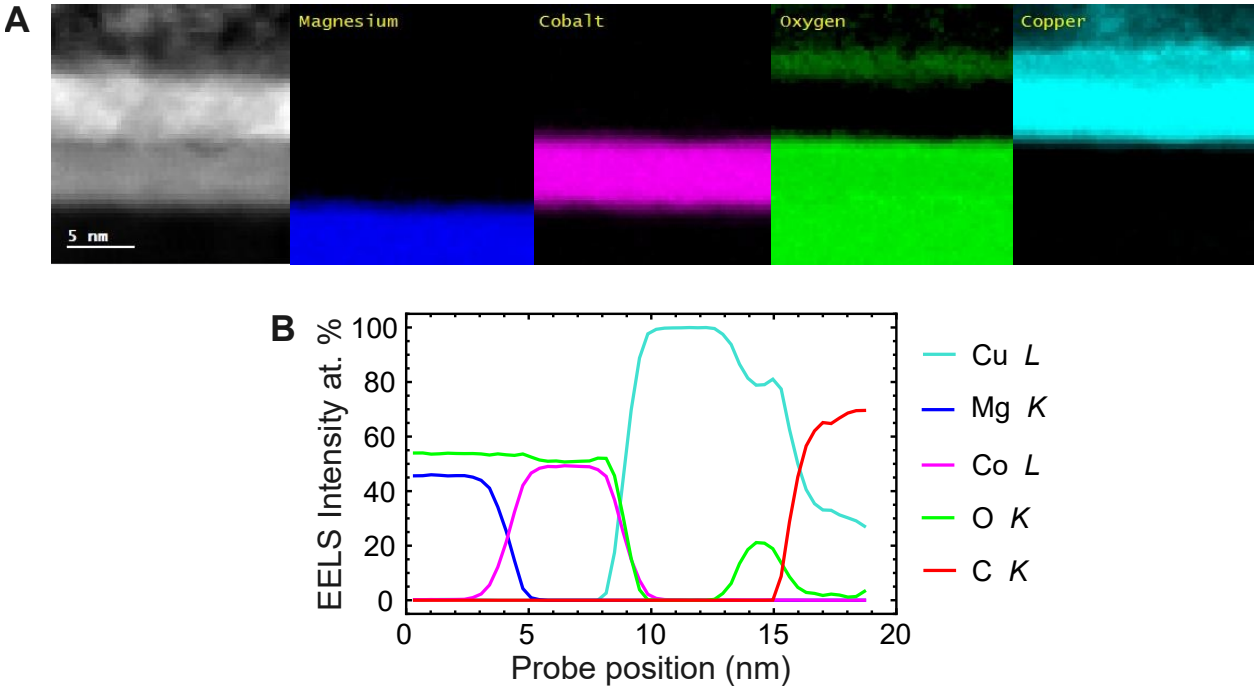

Figure S3: **(A)** HAADF-STEM image and corresponding elemental EELS maps of Mg (blue), Co (pink), O (green) and Cu (turquoise). **(B)** Atomic fraction profiles along the growth direction.

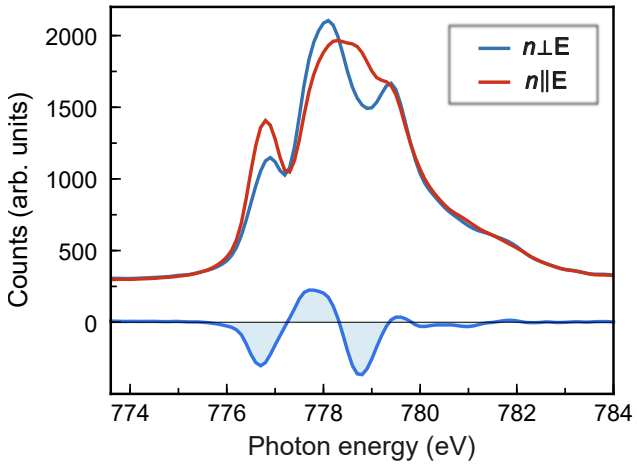

Figure S4: XAS measurements at the Co L_3 edge for two 90° different orientations of the Néel vector $\boldsymbol{n}$ with respect to the X-ray polarization $\boldsymbol{E}$.

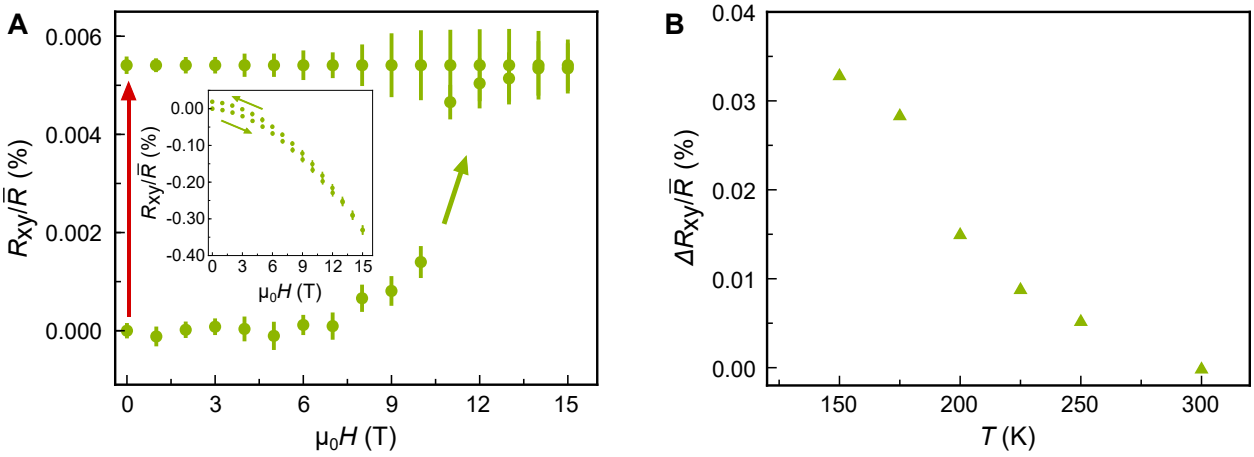

Figure S5: **(A)** Normalized $R_{xy}/\bar{R}$, i.e. OMR, as a function of in-plane magnetic field in a CoO/Cr sample at a temperature, $T = 250$ K. The $R_{xy}/\bar{R}$ exhibits abrupt changes at ≈11 T field, corresponding to the spin-flop field of CoO. The inset shows the raw data with a parabolic background signal arising from Cr. **(B)** The OMR in CoO/Cr as a function of temperature.

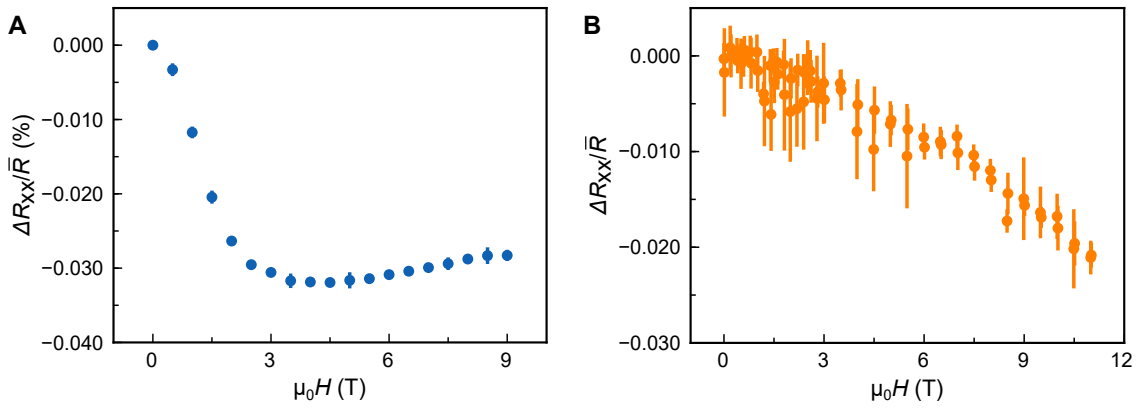

Figure S6: **Interaction of spin and orbital currents with spin-dominated AFM $\alpha - Fe_2O_3$.** Longitudinal resistance of hematite **(A)** Pt and **(B)** Cu* bilayers at 175 K in the easy-axis phase for a magnetic field applied along the current direction.

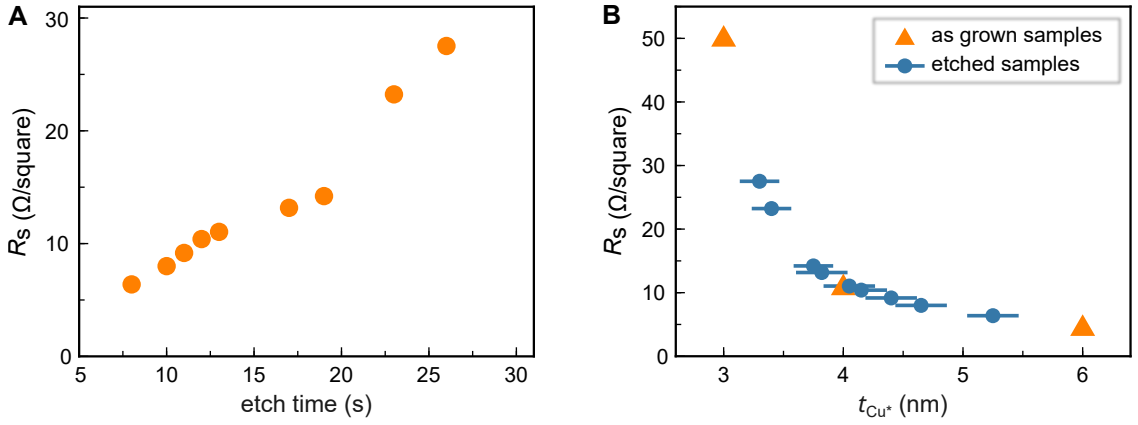

Figure S7: **Thickness calibration of etched Cu* using resistivity measurements.** **(A)** Sheet resistance R_S of the etched Hall bar device as a function of etch time. **(B)** Comparison of sheet resistance of as-grown films with varying Cu* thickness and the sheet resistance of a Cu* layer after several Ar-ion etching steps.

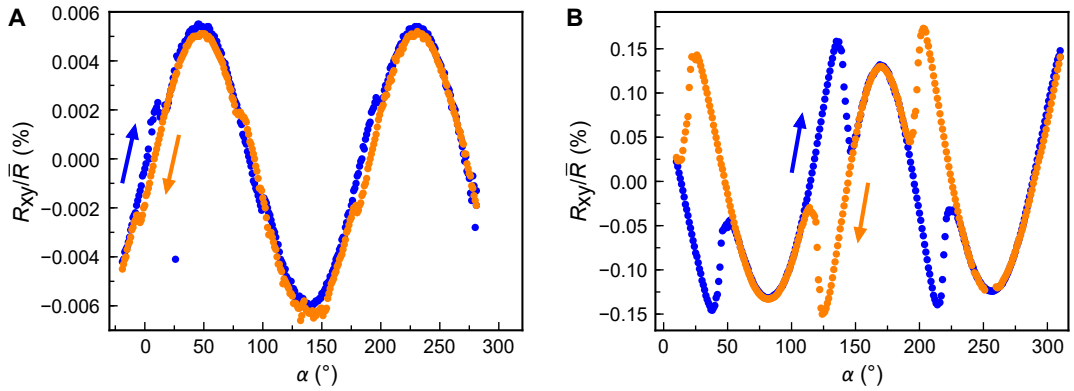

Figure S8: **Angular dependence of transverse spin and orbital magnetoresistance in CoO.** Angular dependence of transverse magnetoresistance in **(A)** CoO/Pt and **(B)** CoO/Cu* at 200 K for an applied magnetic field of 11 T. The blue and orange data points represent two different rotation directions, as indicated by the coloured arrows.

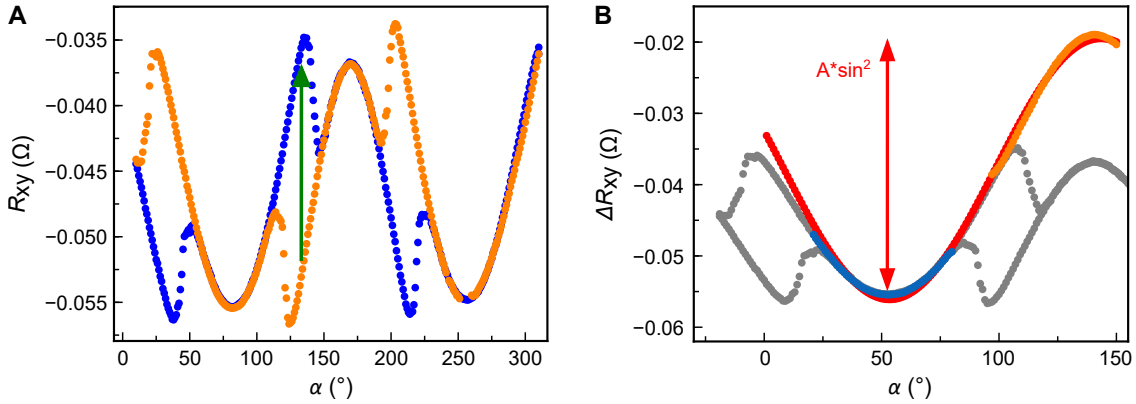

Figure S9: **Disentangling magnetic and spurious contributions to OMR in CoO/Cu***. Exemplary data of CoO/Cu* to show how the two contributions to the signal can be disentangled. **(A)** The amplitude of the hysteretic signal can be determined by shifting one angle sweep direction (orange) of the hysteresis to the second one (blue), as shown by the green arrow. **(B)** By fitting a $sin^2(x)$-function (red) to the minimum and maximum for positive and negative sweep direction (blue and orange) the amplitude of the sinusoidal signal is determined.

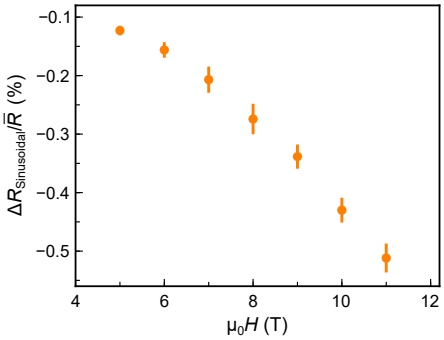

Figure S10: **Field dependence of spurious contribution to OMR in CoO/Cu*.** Amplitudes of the sinusoidal signal as a function of applied magnetic field.

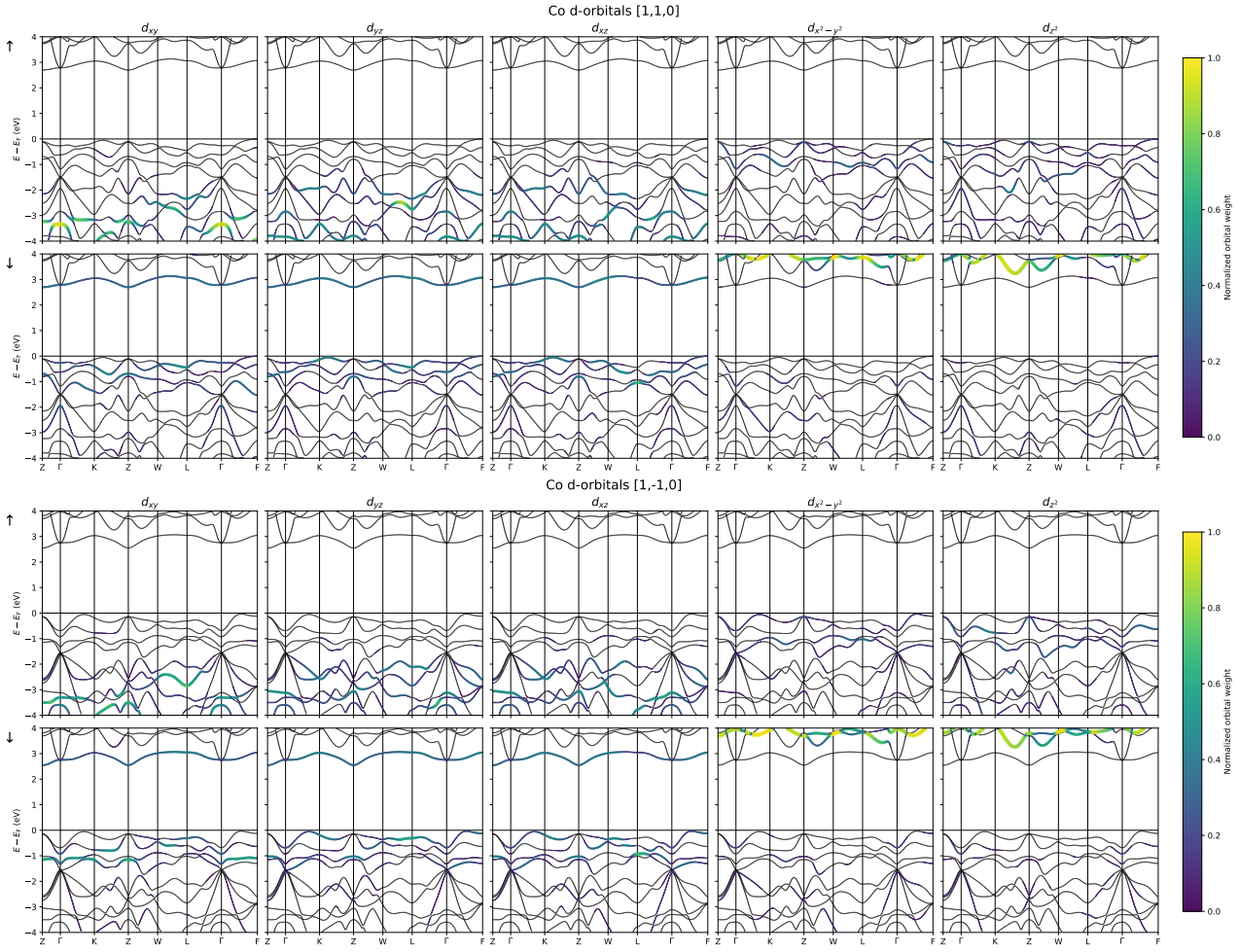

Figure S11: Orbitally-resolved electronic structure of CoO from density functional theory for [110] and [1$\bar{1}$0] directions of the Néel vector.

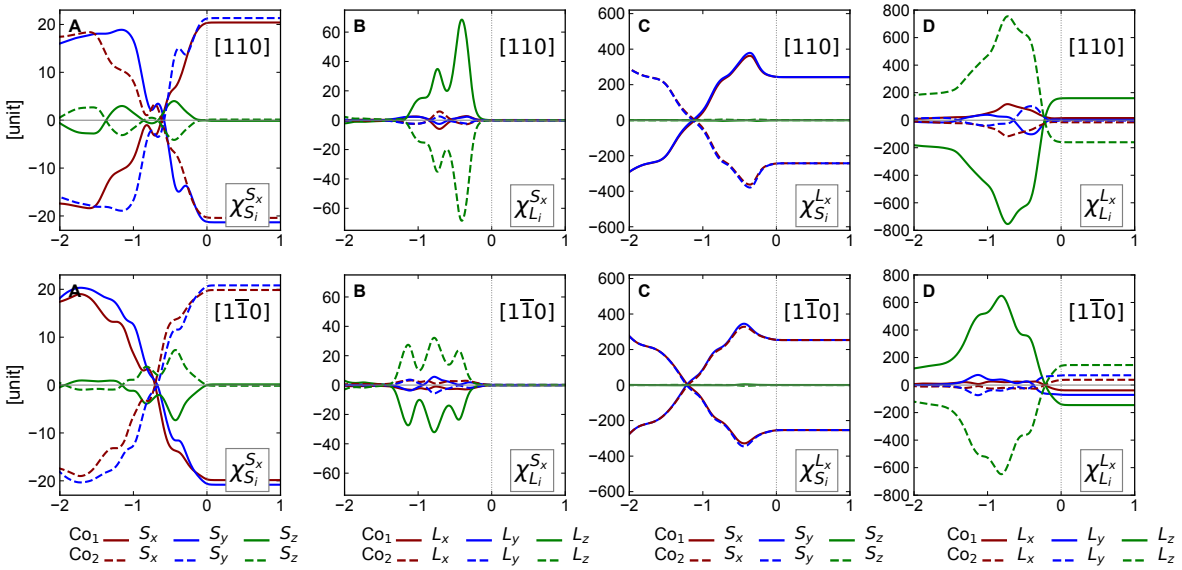

Figure S12: Atomic Co-resolved response of components of spin S_i and orbital L_i angular momentum to an applied along x ([100]) spin (marked with $\chi^{S_x}_{S_i}$ and $\chi^{S_x}_{L_i}$) and orbital ($\chi^{L_x}_{S_i}$ and $\chi^{L_x}_{L_i}$) exchange field, as given by $\chi^{S}_{S(L),ix}$ and $\chi^{L}_{S(L),ix}$, for [110] (upper row) and [1$\bar{1}$0] directions of the Néel vector. The values are in arbitrary units comparable across all plots.

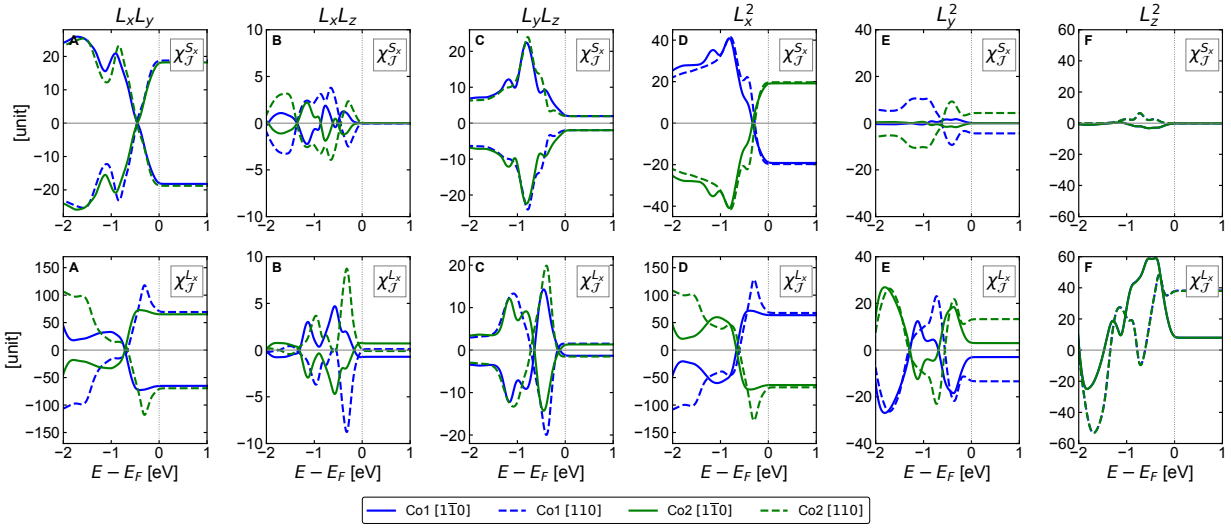

Figure S13: Atomic Co-resolved response of orbital quadrupoles to spin (marked with $\chi^{S_x}_{\mathcal{J}}$, upper panel) and orbital (marked with $\chi^{L_x}_{\mathcal{J}}$, lower panel) exchange field applied along x ([100]), as given by $\chi^{S}_{\mathcal{J},ix}$ and $\chi^{L}_{\mathcal{J},ix}$, where $\mathcal{J}_i = \left(\{L_x, L_y\}, \{L_x, L_z\}, \{L_y, L_z\}, L_x^2, L_y^2, L_z^2\right)$ for [110] and [1$\bar{1}$0] directions of the Néel vector. The values are in arbitrary units comparable across all plots.

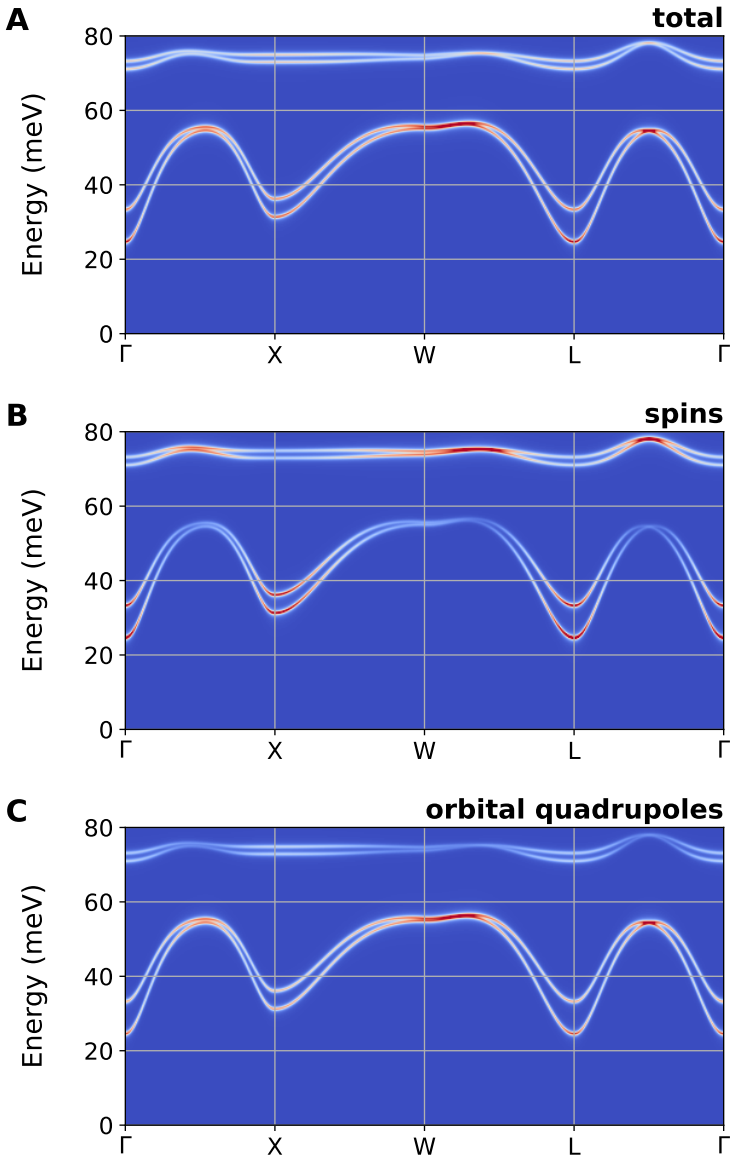

Figure S14: Excitations in the bulk CoO calculated from the effective Hamiltonian (S11). We display the absorptive part of the generalized susceptibility $\bar{\chi}(\mathbf{q}, E)$ traced over all sites and spin-orbital operators **(A)** as well as the partial traces of $\bar{\chi}(\mathbf{q}, E)$ over the spin **(B)** and orbital quadrupole **(C)** subblocks. The high-symmetry points of the parent fcc lattice are $\Gamma = [0, 0, 0]$, $X = [0, 1, 0]$, $W = [1/2, 1, 0]$, $L = [1/2, 1/2, 1/2]$ in the units of $2\pi/a$.

References and Notes

1. M. N. Baibich, J. M. Broto, A. Fert, F. Petroff, P. Etienne, G. Creuzet, A. Friederich, J. Chazelas, J. Chazelas, F. Nguyen Van Dau, Giant magnetoresistance of (001)Fe/(001)Cr magnetic superlattices. *Phys. Rev. Lett.* **61**, 2472–2475 (1988). doi:10.1103/PhysRevLett.61.2472 Medline

2. G. Binasch, P. Grünberg, F. Saurenbach, W. Zinn, Enhanced magnetoresistance in layered magnetic structures with antiferromagnetic interlayer exchange. *Phys. Rev. B* **39**, 4828–4830 (1989). doi:10.1103/PhysRevB.39.4828 Medline

3. I. M. Miron, K. Garello, G. Gaudin, P.-J. Zermatten, M. V. Costache, S. Auffret, S. Bandiera, B. Rodmacq, A. Schuhl, P. Gambardella, Perpendicular switching of a single ferromagnetic layer induced by in-plane current injection. *Nature* **476**, 189–193 (2011). doi:10.1038/nature10309 Medline

4. S. Bhatti, R. Sbiaa, A. Hirohata, H. Ohno, S. Fukami, S. N. Piramanayagam, Spintronics based random access memory: A review. *Mater. Today* **20**, 530–548 (2017). doi:10.1016/j.mattod.2017.07.007

5. A. Fert, V. Cros, J. Sampaio, Skyrmions on the track. *Nat. Nanotechnol.* **8**, 152–156 (2013). doi:10.1038/nnano.2013.29 Medline

6. K. Everschor-Sitte, J. Masell, R. M. Reeve, M. Kläui, Perspective: Magnetic skyrmionsâ€"Overview of recent progress in an active research field. *J. Appl. Phys.* **124**, 240901 (2018). doi:10.1063/1.5048972

7. X. Zhang, M. Ezawa, Y. Zhou, Magnetic skyrmion logic gates: Conversion, duplication and merging of skyrmions. *Sci. Rep.* **5**, 9400 (2015). doi:10.1038/srep09400 Medline

8. J. Grollier, D. Querlioz, K. Y. Camsari, K. Everschor-Sitte, S. Fukami, M. D. Stiles, Neuromorphic Spintronics. *Nat. Electron.* **3**, 360–370 (2020). doi:10.1038/s41928-019-0360-9 Medline

9. T. da Câmara Santa Clara Gomes, Y. Sassi, D. Sanz-Hernández, S. Krishnia, S. Collin, M.-B. Martin, P. Seneor, V. Cros, J. Grollier, N. Reyren, Neuromorphic weighted sums with magnetic skyrmions. *Nat. Electron.* **8**, 204–214 (2025). doi:10.1038/s41928-024-01303-z

10. G. Beneke, T. B. Winkler, K. Raab, M. A. Brems, F. Kammerbauer, P. Gerhards, K. Knobloch, S. Krishnia, J. H. Mentink, M. Kläui, Gesture recognition with Brownian reservoir computing using geometrically confined skyrmion dynamics. *Nat. Commun.* **15**, 8103 (2024). doi:10.1038/s41467-024-52345-y Medline

11. A. Manchon, J. Železný, I. M. Miron, T. Jungwirth, J. Sinova, A. Thiaville, K. Garello, P. Gambardella, Current-induced spin-orbit torques in ferromagnetic and antiferromagnetic systems. *Rev. Mod. Phys.* **91**, 035004 (2019). doi:10.1103/RevModPhys.91.035004

12. D. Go, D. Jo, H.-W. Lee, M. Kläui, Y. Mokrousov, Orbitronics: Orbital currents in solids. *Europhys. Lett.* **135**, 37001 (2021). doi:10.1209/0295-5075/ac2653

13. D. Go, D. Jo, C. Kim, H.-W. Lee, Intrinsic Spin and Orbital Hall Effects from Orbital Texture. *Phys. Rev. Lett.* **121**, 086602 (2018). doi:10.1103/PhysRevLett.121.086602 Medline

14. S. Ding, A. Ross, D. Go, L. Baldrati, Z. Ren, F. Freimuth, S. Becker, F. Kammerbauer, J. Yang, G. Jakob, Y. Mokrousov, M. Kläui, Harnessing Orbital-to-Spin Conversion of Interfacial Orbital Currents for Efficient Spin-Orbit Torques. *Phys. Rev. Lett.* **125**, 177201 (2020). doi:10.1103/PhysRevLett.125.177201 Medline

15. K.-J. Lee, V. Cros, H.-W. Lee, Electric-field-induced orbital angular momentum in metals. *Nat. Mater.* **23**, 1302–1304 (2024). doi:10.1038/s41563-024-01978-x Medline

16. S. Fukami, K.-J. Lee, M. Kläui, Challenges and opportunities in orbitronics. *Nat. Phys.* (2025). doi:10.1038/s41567-025-03143-w

17. T. Tanaka, H. Kontani, M. Naito, T. Naito, D. S. Hirashima, K. Yamada, J. Inoue, Intrinsic spin Hall effect and orbital Hall effect in 4*d* 5*d*. *Phys. Rev. B* **77**, 165117 (2008). doi:10.1103/PhysRevB.77.165117

18. H. Kontani, T. Tanaka, D. S. Hirashima, K. Yamada, J. Inoue, Giant orbital Hall effect in transition metals: Origin of large spin and anomalous Hall effects. *Phys. Rev. Lett.* **102**, 016601 (2009). doi:10.1103/PhysRevLett.102.016601 Medline

19. A. Johansson, B. Göbel, J. Henk, M. Bibes, I. Mertig, Spin and orbital Edelstein effects in a two-dimensional electron gas: Theory and application to $SrTiO_3$. *Phys. Rev. Res.* **3**, 013275 (2021). doi:10.1103/PhysRevResearch.3.013275

20. S. A. Nikolaev, M. Chshiev, F. Ibrahim, S. Krishnia, N. Sebe, J.-M. George, V. Cros, H. Jaffrès, A. Fert, Large Chiral Orbital Texture and Orbital Edelstein Effect in Co/Al Heterostructure. *Nano Lett.* **24**, 13465–13472 (2024). doi:10.1021/acs.nanolett.4c01607 Medline

21. A. Fert, R. Ramesh, V. Garcia, F. Casanova, M. Bibes, Electrical control of magnetism by electric field and current-induced torques. *Rev. Mod. Phys.* **96**, 015005 (2024). doi:10.1103/RevModPhys.96.015005

22. L. Salemi, P. M. Oppeneer, First-principles theory of intrinsic spin and orbital Hall and Nernst effects in metallic monoatomic crystals. *Phys. Rev. Mater.* **6**, 095001 (2022). doi:10.1103/PhysRevMaterials.6.095001

23. S. Krishnia, Y. Sassi, F. Ajejas, N. Sebe, N. Reyren, S. Collin, T. Denneulin, A. Kovács, R. E. Dunin-Borkowski, A. Fert, J.-M. George, V. Cros, H. Jaffrès, Large Interfacial Rashba Interaction Generating Strong Spin-Orbit Torques in Atomically Thin Metallic Heterostructures. *Nano Lett.* **23**, 6785–6791 (2023). doi:10.1021/acs.nanolett.2c05091 Medline

24. Y.-G. Choi, D. Jo, K.-H. Ko, D. Go, K.-H. Kim, H. G. Park, C. Kim, B.-C. Min, G.-M. Choi, H.-W. Lee, Observation of the orbital Hall effect in a light metal Ti. *Nature* **619**, 52–56 (2023). doi:10.1038/s41586-023-06101-9 Medline

25. I. Lyalin, S. Alikhah, M. Berritta, P. M. Oppeneer, R. K. Kawakami, Magneto-Optical Detection of the Orbital Hall Effect in Chromium. *Phys. Rev. Lett.* **131**, 156702 (2023). doi:10.1103/PhysRevLett.131.156702 Medline

26. A. Bose, F. Kammerbauer, R. Gupta, D. Go, Y. Mokrousov, G. Jakob, M. Kläui, Detection of long-range orbital-Hall torques. *Phys. Rev. B* **107**, 134423 (2023). doi:10.1103/PhysRevB.107.134423

27. S. Krishnia, B. Bony, E. Rongione, L. M. Vicente-Arche, T. Denneulin, A. Pezo, Y. Lu, R. E. Dunin-Borkowski, S. Collin, A. Fert, J.-M. George, N. Reyren, V. Cros, H. Jaffrès, Quantifying the large contribution from orbital Rashba–Edelstein effect to the effective damping-like torque on magnetization. *APL Mater.* **12**, 051105 (2024). doi:10.1063/5.0198970

28. G. Sala, P. Gambardella, Giant orbital Hall effect and orbital-to-spin conversion in 3*d* 5*d* 4*f*. *Phys. Rev. Res.* **4**, 033037 (2022). doi:10.1103/PhysRevResearch.4.033037

29. R. Gupta, C. Bouard, F. Kammerbauer, J. O. Ledesma-Martin, A. Bose, I. Kononenko, S. Martin, P. Usé, G. Jakob, M. Drouard, M. Kläui, Harnessing orbital Hall effect in spin-orbit torque MRAM. *Nat. Commun.* **16**, 130 (2025). doi:10.1038/s41467-024-55437-x Medline

30. M. I. Katsnelson, Y. O. Kvashnin, V. V. Mazurenko, A. I. Lichtenstein, Correlated band theory of spin and orbital contributions to Dzyaloshinskii-Moriya interactions. *Phys. Rev. B* **82**, 100403 (2010). doi:10.1103/PhysRevB.82.100403

31. E. Rongione, O. Gueckstock, M. Mattern, O. Gomonay, H. Meer, C. Schmitt, R. Ramos, T. Kikkawa, M. Mičica, E. Saitoh, J. Sinova, H. Jaffrès, J. Mangeney, S. T. B. Goennenwein, S. Geprägs, T. Kampfrath, M. Kläui, M. Bargheer, T. S. Seifert, S. Dhillon, R. Lebrun, Emission of coherent THz magnons in an antiferromagnetic insulator triggered by ultrafast spin-phonon interactions. *Nat. Commun.* **14**, 1818 (2023). doi:10.1038/s41467-023-37509-6 Medline

32. T. Kampfrath, A. Sell, G. Klatt, A. Pashkin, S. Mährlein, T. Dekorsy, M. Wolf, M. Fiebig, A. Leitenstorfer, R. Huber, Coherent terahertz control of antiferromagnetic spin waves. *Nat. Photonics* **5**, 31–34 (2011). doi:10.1038/nphoton.2010.259

33. R. Lebrun, A. Ross, S. A. Bender, A. Qaiumzadeh, L. Baldrati, J. Cramer, A. Brataas, R. A. Duine, M. Kläui, Tunable long-distance spin transport in a crystalline antiferromagnetic iron oxide. *Nature* **561**, 222–225 (2018). doi:10.1038/s41586-018-0490-7 Medline

34. S. Das, A. Ross, X. X. Ma, S. Becker, C. Schmitt, F. van Duijn, E. F. Galíndez-Ruales, F. Fuhrmann, M.-A. Syskaki, U. Ebels, V. Baltz, A.-L. Barra, H. Y. Chen, G. Jakob, S. X. Cao, J. Sinova, O. Gomonay, R. Lebrun, M. Kläui, Anisotropic long-range spin transport in canted antiferromagnetic orthoferrite $YFeO_3$. *Nat. Commun.* **13**, 6140 (2022). doi:10.1038/s41467-022-33520-5 Medline

35. M. R. Norman, Orbital polarization and the insulating gap in the transition-metal oxides. *Phys. Rev. Lett.* **64**, 1162–1165 (1990). doi:10.1103/PhysRevLett.64.1162 Medline

36. C. T. Chen, Y. U. Idzerda, H. Lin, N. V. Smith, G. Meigs, E. Chaban, G. H. Ho, E. Pellegrin, F. Sette, Experimental confirmation of the X-ray magnetic circular dichroism sum rules for iron and cobalt. *Phys. Rev. Lett.* **75**, 152–155 (1995). doi:10.1103/PhysRevLett.75.152 Medline

37. S. Krishnia, L. Vojáček, T. C. S. C. Gomes, N. Sebe, F. Ibrahim, J. Li, L. M. Vicente-Arche, S. Collin, T. Denneulin, R. E. Dunin-Borkowski, S. A. Nikolaev, P. Ohresser, N. Jaouen, A. Thiaville, A. Fert, H. Jaffrès, M. Chshiev, N. Reyren, V. Cros, Interfacial spin-orbitronic effects controlled by different oxidation levels at the CO / A1 interface. *Phys. Rev. Appl.* **24**, 024055 (2025). doi:10.1103/gtwk-mq1y

38. M. Grzybowski, C. F. Schippers, O. Gomonay, K. Rubi, M. E. Bal, U. Zeitler, A. Kozioł-Rachwał, M. Szpytma, W. Janus, B. Kurowska, S. Kret, M. Gryglas-Borysiewicz, B. Koopmans, H. J. M. Swagten, Antiferromagnetic hysteresis above the spin-flop field. *Phys. Rev. B* **107**, L060403 (2023). doi:10.1103/PhysRevB.107.L060403

39. W. Wang, T. Wang, V. P. Amin, Y. Wang, A. Radhakrishnan, A. Davidson, S. R. Allen, T. J. Silva, H. Ohldag, D. Balzar, B. L. Zink, P. M. Haney, J. Q. Xiao, D. G. Cahill, V. O. Lorenz, X. Fan, Anomalous spin-orbit torques in magnetic single-layer films. *Nat. Nanotechnol.* **14**, 819–824 (2019). doi:10.1038/s41565-019-0504-0 Medline

40. S. Krishnia, E. Haltz, L. Berges, L. Aballe, M. Foerster, L. Bocher, R. Weil, A. Thiaville, J. Sampaio, A. Mougin, Spin-Orbit Coupling in Single-Layer Ferrimagnets: Direct Observation of Spin-Orbit Torques and Chiral Spin Textures. *Phys. Rev. Appl.* **16**, 024040 (2021). doi:10.1103/PhysRevApplied.16.024040

41. Materials and methods are available in the supplementary materials.

42. L. Baldrati, C. Schmitt, O. Gomonay, R. Lebrun, R. Ramos, E. Saitoh, J. Sinova, M. Kläui, Efficient spin torques in antiferromagnetic CoO/Pt quantified by comparing field-and current-induced switching. *Phys. Rev. Lett.* **125**, 077201 (2020). doi:10.1103/PhysRevLett.125.077201 Medline

43. C. Schmitt, A. Rajan, G. Beneke, A. Kumar, T. Sparmann, H. Meer, B. Bednarz, R. Ramos, M. A. Niño, M. Foerster, E. Saitoh, M. Kläui, Mechanisms of Electrical Switching of Ultrathin CoO/Pt Bilayers. *Nano Lett.* **24**, 1471–1476 (2024). doi:10.1021/acs.nanolett.3c02890 Medline

44. W. Roth, Magnetic structures of MnO, FeO, CoO, and NiO. *Phys. Rev.* **110**, 1333–1341 (1958). doi:10.1103/PhysRev.110.1333

45. S. Saito, K. Nakahigashi, Y. Shimomura, X-ray diffraction study on CoO. *J. Phys. Soc. Jpn.* **21**, 850–860 (1966). doi:10.1143/JPSJ.21.850

46. H. Nakayama, M. Althammer, Y.-T. Chen, K. Uchida, Y. Kajiwara, D. Kikuchi, T. Ohtani, S. Geprägs, M. Opel, S. Takahashi, R. Gross, G. E. W. Bauer, S. T. B. Goennenwein, E. Saitoh, Spin Hall magnetoresistance induced by a nonequilibrium proximity effect. *Phys. Rev. Lett.* **110**, 206601 (2013). doi:10.1103/PhysRevLett.110.206601 Medline

47. J. Kim, P. Sheng, S. Takahashi, S. Mitani, M. Hayashi, Spin Hall Magnetoresistance in Metallic Bilayers. *Phys. Rev. Lett.* **116**, 097201 (2016). doi:10.1103/PhysRevLett.116.097201 Medline

48. S. Ding, Z. Liang, D. Go, C. Yun, M. Xue, Z. Liu, S. Becker, W. Yang, H. Du, C. Wang, Y. Yang, G. Jakob, M. Kläui, Y. Mokrousov, J. Yang, Observation of the Orbital Rashba-Edelstein Magnetoresistance. *Phys. Rev. Lett.* **128**, 067201 (2022). doi:10.1103/PhysRevLett.128.067201 Medline

49. S. Vélez, V. N. Golovach, A. Bedoya-Pinto, M. Isasa, E. Sagasta, M. Abadia, C. Rogero, L. E. Hueso, F. S. Bergeret, F. Casanova, Hanle magnetoresistance in thin metal films with strong spin-orbit coupling. *Phys. Rev. Lett.* **116**, 016603 (2016). doi:10.1103/PhysRevLett.116.016603 Medline

50. G. R. Hoogeboom, A. Aqeel, T. Kuschel, T. Palstra, B. J. van Wees, Negative spin Hall magnetoresistance of Pt on the bulk easy-plane antiferromagnet NiO. *Appl. Phys. Lett.* **111**, 052409 (2017). doi:10.1063/1.4997588

51. S. R. Marmion, M. Ali, M. McLaren, D. A. Williams, B. J. Hickey, Temperature dependence of spin Hall magnetoresistance in thin YIG/Pt films. *Phys. Rev. B* **89**, 220404 (2014). doi:10.1103/PhysRevB.89.220404

52. J.-Y. Yoon, P. Zhang, C.-T. Chou, Y. Takeuchi, T. Uchimura, J. T. Hou, J. Han, S. Kanai, H. Ohno, S. Fukami, L. Liu, Handedness anomaly in a noncollinear antiferromagnet under spin-orbit torque. *Nat. Mater.* **22**, 1106–1113 (2023). doi:10.1038/s41563-023-01620-2 Medline

53. I. V. Solovyev, A. I. Liechtenstein, K. Terakura, Is Hund's Second Rule Responsible for the Orbital Magnetism in Solids? *Phys. Rev. Lett.* **80**, 5758–5761 (1998). doi:10.1103/PhysRevLett.80.5758

54. A. Boussendel, N. Baadji, A. Haroun, H. Dreyssé, M. Alouani, Effect of substrate strain on calculated magnetic properties and magnetic anisotropy energy of CoO. *Phys. Rev. B* **81**, 184432 (2010). doi:10.1103/PhysRevB.81.184432

55. S. Han, D. Jo, I. Baek, S. Cheon, P. M. Oppeneer, H.-W. Lee, Harnessing magnetic octupole Hall effect to induce torque in altermagnets. *Phys. Rev. Lett.* **135**, 076705 (2025). doi:10.1103/lxkx-ypbg Medline

56. C. Schmitt, S. Krishnia, M. Zeer, E. Galíndez-Ruales, M. Loyal, J. Köhler, L. Micus, T. Kikkawa, H. Arisawa, T. Denneulin, A. Kovács, R. Xu, D. Tran, F. Kronast, D. Go, L. V. Pourovskii, R. E. Dunin-Borkowski, T. Kuschel, M. Lezaic, J. Sinova, E. Saitoh, G. Jakob, O. Gomonay, Y. Mokrousov, M. Kläui, Data for: Orbital magnetoresistance in the antiferromagnet CoO driven by dynamic orbital angular momentum, Version 1 (Zenodo, 2026); https://doi.org/10.5281/zenodo.18860804.

57. S. I. Csiszar, M. W. Haverkort, Z. Hu, A. Tanaka, H. H. Hsieh, H.-J. Lin, C. T. Chen, T. Hibma, L. H. Tjeng, Controlling orbital moment and spin orientation in CoO layers by strain. *Phys. Rev. Lett.* **95**, 187205 (2005). doi:10.1103/PhysRevLett.95.187205 Medline

58. R. Abrudan, J. Miguel, M. Bernien, C. Tieg, M. Piantek, J. Kirschner, W. Kuch, Structural and magnetic properties of epitaxial Fe/ CoO bilayers on Ag (001). *Phys. Rev. B* **77**, 014411 (2008). doi:10.1103/PhysRevB.77.014411

59. F. De Groot, A. Kotani, *Core Level Spectroscopy of Solids* (CRC press, 2008).

60. G. van der Laan, Magnetic linear x-ray dichroism as a probe of the magnetocrystalline anisotropy. *Phys. Rev. Lett.* **82**, 640–643 (1999). doi:10.1103/PhysRevLett.82.640

61. G. Rollmann, A. Rohrbach, P. Entel, J. Hafner, First-principles calculation of the structure and magnetic phases of hematite. *Phys. Rev. B* **69**, 165107 (2004). doi:10.1103/PhysRevB.69.165107

62. A. Ross, R. Lebrun, C. Ulloa, D. A. Grave, A. Kay, L. Baldrati, F. Kronast, S. Valencia, A. Rothschild, M. Kläui, Structural sensitivity of the spin Hall magnetoresistance in antiferromagnetic thin films. *Phys. Rev. B* **102**, 094415 (2020). doi:10.1103/PhysRevB.102.094415

63. L. Pauw, A method of measuring specific resistivity and Hall effect of discs of arbitrary shape. *Philips Res. Rep.* **13**, 1–9 (1958).

64. D. Wortmann, G. Michalicek, N. Baadji, W. Beida, M. Betzinger, G. Bihlmayer, T. Bornhake, J. Bröder, T. Burnus, J. Enkovaara, F. Freimuth, C. Friedrich, C.-R. Gerhorst, S. Granberg Cauchi, U. Grytsiuk, A. Hanke, J.-P. Hanke, M. Heide, S. Heinze, R. Hilgers, H. Janssen, D. A. Klüppelberg, R. Kovacik, P. Kurz, M. Lezaic, G. K. H. Madsen, Y. Mokrousov, A. Neukirchen, M. Redies, S. Rost, M. Schlipf, A. Schindlmayr, M. Winkelmann, S. Blügel, FLEUR, Version MaX-R7.2, Zenodo (2023); https://doi.org/10.5281/zenodo.13833162.

65. J. P. Perdew, K. Burke, M. Ernzerhof, Generalized Gradient Approximation Made Simple. *Phys. Rev. Lett.* **77**, 3865–3868 (1996). doi:10.1103/PhysRevLett.77.3865 Medline

66. A. Georges, G. Kotliar, W. Krauth, M. J. Rozenberg, Dynamical mean-field theory of strongly correlated fermion systems and the limit of infinite dimensions. *Rev. Mod. Phys.* **68**, 13–125 (1996). doi:10.1103/RevModPhys.68.13

67. V. I. Anisimov, A. I. Poteryaev, M. A. Korotin, A. O. Anokhin, G. Kotliar, First-principles calculations of the electronic structure and spectra of strongly correlated systems: Dynamical mean-field theory. *J. Phys. Condens. Matter* **9**, 7359–7367 (1997). doi:10.1088/0953-8984/9/35/010

68. A. I. Lichtenstein, M. I. Katsnelson, Ab initio calculations of quasiparticle band structure in correlated systems: LDA++ approach. *Phys. Rev. B* **57**, 6884–6895 (1998). doi:10.1103/PhysRevB.57.6884

69. J. Hubbard, Electron correlations in narrow energy bands. *Proc. R. Soc.* **276**, 238–257 (1963). doi:10.1098/rspa.1963.0204

70. L. V. Pourovskii, Two-site fluctuations and multipolar intersite exchange interactions in strongly correlated systems. *Phys. Rev. B* **94**, 115117 (2016). doi:10.1103/PhysRevB.94.115117

71. M. Aichhorn, L. Pourovskii, V. Vildosola, M. Ferrero, O. Parcollet, T. Miyake, A. Georges, S. Biermann, Dynamical mean-field theory within an augmented plane-wave framework: Assessing electronic correlations in the iron pnictide LaFeAsO. *Phys. Rev. B* **80**, 085101 (2009). doi:10.1103/PhysRevB.80.085101

72. M. Aichhorn, L. V. Pourovskii, A. Georges, Importance of electronic correlations for structural and magnetic properties of the iron pnictide superconductor LaFeAsO. *Phys. Rev. B* **84**, 054529 (2011). doi:10.1103/PhysRevB.84.054529

73. M. Aichhorn, L. Pourovskii, P. Seth, V. Vildosola, M. Zingl, O. E. Peil, X. Deng, J. Mravlje, G. J. Kraberger, C. Martins, M. Ferrero, O. Parcollet, TRIQS/DFTTools: A TRIQS application for ab initio calculations of correlated materials. *Comput. Phys. Commun.* **204**, 200–208 (2016). doi:10.1016/j.cpc.2016.03.014

74. P. Blaha, K. Schwarz, G.K.H. Madsen, D. Kvasnicka, J. Luitz, R. Laskowski, F. Tran, L.D. Marks, *WIEN2k, An Augmented Plane Wave + Local Orbitals Program for Calculating Crystal Properties* (Technique Universitat, Wien, Austria) (2018); http://susi.theochem.tuwien.ac.at/.

75. O. Parcollet, M. Ferrero, T. Ayral, H. Hafermann, I. Krivenko, L. Messio, P. Seth, TRIQS: A toolbox for research on interacting quantum systems. *Comput. Phys. Commun.* **196**, 398–415 (2015). doi:10.1016/j.cpc.2015.04.023

76. B. Amadon, F. Lechermann, A. Georges, F. Jollet, T. O. Wehling, A. I. Lichtenstein, Plane-wave based electronic structure calculations for correlated materials using dynamical mean-field theory and projected local orbitals. *Phys. Rev. B* **77**, 205112 (2008). doi:10.1103/PhysRevB.77.205112

77. B.-C. Shih, T. A. Abtew, X. Yuan, W. Zhang, P. Zhang, Screened Coulomb interactions of localized electrons in transition metals and transition-metal oxides. *Phys. Rev. B* **86**, 165124 (2012). doi:10.1103/PhysRevB.86.165124

78. V. I. Anisimov, I. V. Solovyev IV, M. A. Korotin, M. T. Czyżyk, G. A. Sawatzky, Density-functional theory and NiO photoemission spectra. *Phys. Rev. B* **48**, 16929–16934 (1993). doi:10.1103/PhysRevB.48.16929 Medline

79. A. Abragam, B. Bleaney, *Electron Paramagnetic Resonance of Transition Ions*, (Clarendon Press, 1970).

80. L. V. Pourovskii, D. Fiore Mosca, MagInteract / MagInt, Github [Accessed 2026]; https://github.com/MagInteract/MagInt.

81. A. Georges, Strongly Correlated Electron Materials: Dynamical Meanâ€• Field Theory and Electronic Structure. *AIP Conf. Proc.* **715**, 3–74 (2004). doi:10.1063/1.1800733

82. G. Kotliar, S. Y. Savrasov, K. Haule, V. S. Oudovenko, O. Parcollet, C. A. Marianetti, Electronic structure calculations with dynamical mean-field theory. *Rev. Mod. Phys.* **78**, 865–951 (2006). doi:10.1103/RevModPhys.78.865

83. L. V. Pourovskii, D. Fiore Mosca, L. Celiberti, S. Khmelevskyi, A. Paramekanti, C. Franchini, Hidden orders in spin–orbit-entangled correlated insulators. *Nat. Rev. Mater.* **10**, 674–696 (2025). doi:10.1038/s41578-025-00824-z

84. W. Jauch, M. Reehuis, H. J. Bleif, F. Kubanek, P. Pattison, Crystallographic symmetry and magnetic structure of CoO. *Phys. Rev. B* **64**, 052102 (2001). doi:10.1103/PhysRevB.64.052102

85. P. Delange, S. Biermann, T. Miyake, L. V. Pourovskii, Crystal-field splittings in rare-earth-based hard magnets: An ab initio approach. *Phys. Rev. B* **96**, 155132 (2017). doi:10.1103/PhysRevB.96.155132

86. R. A. Cowley, W. J. L. Buyers, C. Stock, Z. Yamani, C. Frost, J. W. Taylor, D. Prabhakaran, Neutron scattering investigation of the *d* – *d*. *Phys. Rev. B* **88**, 205117 (2013). doi:10.1103/PhysRevB.88.205117

87. M. Rotter, Using McPhase to calculate magnetic phase diagrams of rare earth compounds. *J. Magn. Magn. Mater.* **272-276**, E481–E482 (2004). doi:10.1016/j.jmmm.2003.12.1394

88. J. Jensen, A. R. Mackintosh, *Rare Earth Magnetism: Structures and Excitations* (Clarendon Press, 1991).

89. M. Rotter, M. D. Le, A. T. Boothroyd, J. A. Blanco, Dynamical matrix diagonalization for the calculation of dispersive excitations. *J. Phys. Condens. Matter* **24**, 213201 (2012). doi:10.1088/0953-8984/24/21/213201 Medline

90. K. Tomiyasu, S. Itoh, Magnetic Excitations in CoO. *J. Phys. Soc. Jpn.* **75**, 084708 (2006). doi:10.1143/JPSJ.75.084708

91. P. M. Sarte, M. Songvilay, E. Pachoud, R. A. Ewings, C. D. Frost, D. Prabhakaran, K. H. Hong, A. J. Browne, Z. Yamani, J. P. Attfield, E. E. Rodriguez, S. D. Wilson, C. Stock, Spin-orbit excitons in CoO. *Phys. Rev. B* **100**, 075143 (2019). doi:10.1103/PhysRevB.100.075143

92. P. M. Sarte, S. D. Wilson, J. P. Attfield, C. Stock, Magnetic fluctuations and the spin-orbit interaction in Mott insulating CoO. *J. Phys. Condens. Matter* **32**, 374011 (2020). doi:10.1088/1361-648X/ab8498 Medline

93. J. Kim, D. Casa, M. H. Upton, T. Gog, Y.-J. Kim, J. F. Mitchell, M. van Veenendaal, M. Daghofer, J. van den Brink, G. Khaliullin, B. J. Kim, Magnetic excitation spectra of Sr2IrO4 probed by resonant inelastic x-ray scattering: Establishing links to cuprate superconductors Sr_2IrO_4. *Phys. Rev. Lett.* **108**, 177003 (2012). doi:10.1103/PhysRevLett.108.177003 Medline